Crystallography Reports, Vol. 47, No. 3, 2002, pp. 347–361. From Kristallografiya, Vol. 47, No. 3, 2002, pp. 391–405.

DIFFRACTION AND SCATTERING OF X-RAY AND SYNCHROTRON RADIATION

To the Memory of Riitta Kurki-Suonio

Indications of the Magnetic State in the Charge Distributions in MnO, CoO, and NiO. I: Para- and Antiferromagnetism of MnO[1]

Jean-Pierre Vidal*, Genevieve Vidal-Valat*,

Kaarle Kurki-Suonio, and Riitta Kurki-Suonio**†**

* *Laboratoire d'Analyse Multipolaire des Repartitions de Charges Experimentales, Université Montpellier 2, 34095 Montpellier Cedex 05, France*

e-mail: jpgvidal@univ-montp2.fr

** *Physics Department, P.O. Box 9, FIN-00014 University of Helsinki, Finland*

Received May 28, 2001

Abstract—X-ray diffraction intensities from MnO and CoO were measured above and below their Néel temperatures and from NiO, below the Néel temperature. To detect possible characteristics of the paramagnetic and antiferromagnetic states of the crystals, the data were subjected to direct multipole analysis of the atomic-charge densities. For MnO, both spherical and nonspherical accumulation-of-charge densities indicate the exchange of the roles played by manganese and oxygen in the magnetic phase transition. Both spherical and nonspherical features characteristic of the ionic nature are inherent in both states. The electron counts of the density peaks correspond to Mn^{2+} and O^{1-}, with the tenth electron of O^{2-} being distributed in a wider region. In the paramagnetic state, there is an electronic Mn–Mn bond which seems to be formed due to coupling with the tenth electron of O^{2-} and builds up a three-dimensional net of the charge density with the "cages" surrounding oxygen atoms. In the antiferromagnetic state, some Mn–Mn bonds disappear, while the preserved nonspherical ionic features enhance the role of oxygen atoms in electronic coupling. © *2002 MAIK "Nauka/Interperiodica".*

INTRODUCTION

There is a growing interest in transition-metal monoxides. The systematic study of their electronic structure can improve the understanding of the metal–oxygen chemistry, provide the basis for important corrosion research and a better understanding of the structural and electronic mechanisms necessary for their widespread use as catalysts and in various high-temperature applications.

This study is focused on three monoxides—MnO, CoO, and NiO—with the simple rock salt structure, sp. gr. *Fm3m* (n^0225). All three monoxides are insulators undergoing the transition from the paramagnetic to the antiferromagnetic state at the Néel temperatures 122, 289, and 523 K, respectively [1]. Antiferromagnetism preceding the transition into the superconducting state is characteristic of high-temperature superconductors. Therefore, the study of these compounds can clarify the role of an oxygen anion in the mechanisms of high-temperature superconductivity.

Among the above three materials, MnO is conceptually the simplest one to deal with because of the pronounced exchange splitting of a Mn^{2+} ($3d_5$) ion resulting in the division of the $3d$ level into the occupied spin-up and the empty spin-down components. The NiO oxide is certainly the most studied one, both experimentally and theoretically, of all the transition metal oxides. For several decades, it served as the benchmark system for understanding the electronic structure of transition metal compounds [2]. It was most difficult to interpret the data on CoO in terms of the common models that seemed to be appropriate for MnO and NiO.

There are numerous publications on these compounds—from the experimental studies of magnetic and dielectric properties (spectroscopic investigations of the electronic structure) and neutron diffraction studies of the magnetic structure to the theoretical treatment of the electronic structure with the use of various sophisticated models suggested to attain better agreement with the observed properties, the structure, and the review articles.

The principal magnetic susceptibilities of MnO single crystals were measured and their temperature dependences were studied in [3]. It was concluded that

† Deceased.

[1] This article was submitted by the authors in English.

1063-7745/02/4703-0347$22.00 © 2002 MAIK "Nauka/Interperiodica"

the antiferromagnetic ordering consisted in the formation of ferromagnetic ⟨111⟩ sheets with antiferromagnetic stacking of the (111) planes. Srinivasan [4] reported high-resolution measurements of magnetic susceptibility near T_N in polycrystalline MnO, CoO, and NiO. Seino [5] performed ultrasonic measurements of sound velocity in an antiferromagnetic MnO single crystal. The observed discontinuities of the magnetic susceptibility and of the elastic constants c_{11} and c_{11}–c_{12} at T_N indicate the first-order phase transition.

Seehra and Helmick [6] measured the dielectric constant of MnO along the ⟨111⟩ direction. The anomaly observed below T_N was attributed to exchange striction. Seehra *et al.* [7] studied the temperature dependence of the static dielectric constant $\varepsilon_{\|}$ of MnO in the electric fields parallel and perpendicular to the spin-easy axis, but they failed to explain the signs and the magnitudes of $\varepsilon_{\|}$ and $\varepsilon_{\perp}$.

Ksendzov *et al.* [8] studied the electronic structure of MnO using the reflection spectra of chemically polished MnO crystals. Drokin *et al.* [9] studied the spectral, temperature, and relaxation characteristics of the photoconductivity of MnO single crystals and came to the conclusion that MnO is a wide-band antiferromagnetic semiconductor.

Lad and Henrich [10] studied photoemission spectra of cleaved MnO single crystals with the use of synchrotron radiation and reported data consistent with the localized Mn 3*d* orbital, which indicates that MnO is an insulator with charge transfer rather than a Mott insulator. Mochizuki *et al.* [11] studied photoluminescence in antiferromagnetic and paramagnetic MnO with the invocation of magnon processes and short-wavelength collective excitations. Fujimori *et al.* [12] used photoemission spectroscopy and obtained for MnO a high energy of *d*-charge transfer from the ligand to Mn indicating the pronounced ionic nature of Mn–O bonding.

McKay and Henrich [13] discussed the structure of valence- and conduction-band levels in NiO based on the experimental photoemission and photoabsorption of single crystals. They concluded that NiO is a Mott insulator whose insulating nature is associated with correlation effects. At the same time, Sawatzky and Allen [14] came to the opposite conclusion based on the photoemission and inverse-photoemission spectroscopy data. Hüfner *et al.* [15] studied the photoemission and inverse-photoemission spectra of thin NiO films grown on Ni substrates. On the basis of these data, the 4.0 eV optical gap in NiO was attributed to the charge-transfer transition O2*p* ⟶ Ni3*d*. Zschech *et al.* [16] studied the fluorescence yield from the photoabsorption spectra of bulk NiO. It was shown that self-absorption induces ~50% error in the coordination number. A thorough study of the optical-gap nature in NiO was performed by Hüfner [2].

New data on CoO were obtained from the studies of X-ray absorption and photoemission spectra. Kim [17] paid attention to surface contamination of CoO samples. Van Elp *et al.* [18] found that CoO is a highly correlated insulator. Okada and Kotani [19] considered the Co 2*p* core level by the methods of X-ray absorption and photoemission in CoO based on the CoO_6-cluster model.

Several theoretical studies of MnO have been undertaken both above and below the Néel temperature (118 K). Kanamori [20] indicated that antiferromagnetism can be caused by the mechanism of superexchange interactions. Mattheiss [21] made an attempt to explain the insulating properties of MnO in both antiferromagnetic and paramagnetic states by calculating energy bands. Terakura *et al.* [22] used another approach to band calculations for MnO. They stated that MnO is an insulator only in those cases where magnetization allows the existence on a particular antiferromagnetic spin structure observed experimentally. Terakura *et al.* [23] made an attempt to derive the electronic structure of insulating antiferromagnetic transition metal compounds by considering them as prototypes of a Mott insulator and using the energy band theory based on the model of local spin-density exchange and correlation.

Hugel and Carabatos [24] used the LCAO method to calculate both the valence band and the lowest conduction band of MnO. A new attempt made by Anisimov *et al.* [25] showed that the band-structure calculations with the use of the corrections for the potential of nonoccupied states provided an adequate description of the available spectral data measured for transition-metal monoxides with strong electron correlations.

Bocquet *et al.* [26] emphasized that the one-electron theory fails to describe the electronic structure of the transition-metal compounds discovered recently. Using the cluster-type charge-transfer model calculation, Bocquet *et al.* [26] managed to reproduce the core-level 2*p* X-ray photoemission spectra of a large number of transition metal oxides and sulfides, including MnO and NiO. They concluded that the basic Mott–Hubbard description of the charge fluctuations becomes invalid and that charge-transfer interactions are the most important for understanding the electronic structure of these compounds.

Nolting *et al.* [27] used the model taking into account the metal 3*d* and the oxygen 2*p* subbands, which explains the temperature-dependent electronic and magnetic properties of transition-metal oxides. They explained different properties by different interband and intraband couplings. The insulating properties require an integral number n of 3*d* electrons exceeding four, whereas antiferromagnetism is caused by $10 - n$ half-filled (exactly) 3*d* subbands and $n - 5$ completely filled subbands. This model correctly predicts the fact that MnO, CoO, and NiO are antiferromagnetic insulators.

Anisimov *et al.* [28] present a scheme for calculating photoemission spectra of transition metal oxides from first principles without any adjustable parameters.

The application of this method to NiO provided good agreement of the calculated and the experimental photoemission spectra and also their consistency with the oxygen K_α X-ray-emission spectra. They also reviewed the alternative approaches for calculating the properties of NiO.

In principle, the most direct means for obtaining the information on the magnetic structure is neutron diffraction. However, Roth [29, 30] indicated that magnetic scattering from polydomain single crystals cannot yield detailed information on the magnetic structure, because the distribution of the magnetization within the unit cell is averaged over the domains. To avoid this shortcoming, Bloch *et al.* [31] used the external mechanical stresses along the [111] direction and the external magnetic field to determine the order-parameter discontinuity in the magnetic transition in MnO.

More recently, Shaked *et al.* [32] studied the antiferromagnetic structure of MnO using high-resolution neutron diffraction from a polycrystalline MnO sample at 8 K. They found that, within the experimental resolution attained, the spin axis is perpendicular to the unique [111] direction.

Hermann-Ronzaud *et al.* [33] performed intense neutron diffraction studies on CoO samples subjected to stresses or magnetic fields to obtain monodomain crystals with the aim of analyzing the antiferromagnetic phase.

Chang *et al.* [34] studied the neutron-scattering factors of antiferromagnetic NiO using the calculations by the cluster model. The calculations took into account asphericity of the spin density around each Ni atom. The data obtained could be compared with the experiment only based on relative formfactor data for NiO. The agreement between the calculated and the experimental parameters depended mainly on the parameter nature.

A few X-ray diffraction studies of the charge densities of these compounds have been performed, but, unfortunately, so far they did not provide a better understanding of the electronic mechanism of magnetic ordering. These studies were performed mainly on the paramagnetic phases of MnO and NiO. The data obtained concern the net atomic charges and their radii.

Kuriyama and Hosoya [35] made an attempt to detect nonsphericities of the atomic charge distributions in MnO by the method of powder diffraction at room temperature. They concluded that both the Mn and O in the structure are in the state of divalent ions. Uno [36] subjected several transition metal monoxides to detailed powder-diffraction studies and tried to find evidence on superexchange atomic interactions. Meisalo and Inkinen [37] analyzed these data more thoroughly by the spherical-partitioning method and came to the conclusion that CoO behavior is essentially different from the behavior of MnO and NiO. Sasaki *et al.* [38] made a new X-ray diffraction study of spherical MnO crystals. They concluded that the ions were in doubly ionized states but were not considerably deformed in comparison with the ions in the free-atom superposition model. In view of the easy deformability of oxygen ions, this fact is a bit surprising.

Encouraged by our earlier experience in precision X-ray diffraction measurements and their direct multipole analysis (see, e.g., [39–41]), we decided to make an attempt to find the evidence of the magnetic states of these compounds by this method and, possibly, some indications to the bonding nature and the electronic mechanisms of the magnetic ordering. With this aim, we made high-accuracy X-ray diffraction measurements on MnO and CoO at 85 and 298 K and on NiO at 298 K, thus covering the antiferromagnetic phases of all three compounds and the paramagnetic phase of the first two compounds, and then performed the multipole analysis of the atomic-charge distributions.

EXPERIMENTAL

1. Sample

A stoichiometric MnO single crystal was kindly provided by the *Laboratoire de Chimie des Solides*, Université d'Orsay, France. It was synthesized by float-zone refining techniques from high-purity 5N powder. In this method, a high degree of mosaicity is provided by minimizing the extinction effect on the diffracted intensities so that the conventional extinction corrections are quite satisfactory, as was stated in [42]. Crystal stoichiometry was checked and confirmed by the optical and crystallographic methods, as is described elsewhere [43].

The crystal was cleaved several times along the (001) crystal faces. It was rather hard and, if sufficiently thin, fully optically transparent and had a bright green color, indicating both its stoichiometry and crystalline quality. The cleavage surface was perfectly smooth. Indeed, the crystalline quality is very important, whereas many studies reported in the literature were performed on poorly crystallized samples. The sample chosen for the X-ray diffraction measurements had the shape of a $0.182 \times 0.152 \times 0.114$-mm^3 parallelepiped. The as-cleaved sample was coated with plastic to avoid its oxidation. This protective film was perfectly transparent to the X-ray beam.

2. Data Collection

A precision X-ray diffraction study of MnO was carried out both above and below the Néel temperature, at 298 K for the paramagnetic phase and at 85 K for the antiferromagnetic one. The temperature was maintained within about 1 K. Neither magnetic field nor mechanical stresses were applied to the sample during X-ray diffraction measurements.

The precision X-ray diffraction measurements on magnetic polydomain crystals show that, at temperatures below the Néel point, the antiferromagnetic dis-

tortion of the NaCl-type structure is not perceptible. All the crystals studied had face-centered cubic lattices.

Roth [30] indicated that the magnetic scattering from a polydomain single crystal cannot be used in the detailed determination of the magnetic structure, since the latter is formed as a consequence of both the distribution of magnetic moments within the unit cell and the distribution of domains present in both powder and single crystal. This argument also holds for X-ray diffraction studies.

Bloch *et al.* [31] suggested avoiding this effect by applying mechanical stresses along the [111] direction, or an external magnetic field, or both. However, in this way, the magnetization of all the domains is forced along the same direction independently of lattice orientations in the domains. Therefore the results obtained are not related to the real crystalline magnetic field. Therefore, we did not apply an external field in our studies. Thus, if our results involve cubic symmetrization, the results obtained relate to the true field in the crystal and not to an artificially distorted one.

The lattice constants 4.431(2) and 4.425(2) Å for MnO at 298 and 85 K, respectively, were obtained by the least-squares refinement based on X-ray diffraction data.

Relative integrated intensities of all the reflections with $\sin\theta/\lambda$ up to about 1 $Å^{-1}$ in three octants were collected three times at both temperatures on an automated four-circle Enraf-Nonius CAD-4 diffractometer (MoK_α radiation). The data thus obtained included 26 independent reflections.

The integration was done in the θ–2θ scan mode with programmed scan and the aperture at the scanning rate of $2^\circ\ s^{-1}$. The dead-time correction was automatically taken into account by the analyzer.

The multiple-scattering effect was eliminated using different settings of the crystallographic and diffractometer axes. As a check, all the forbidden reflections were measured in the whole octant. No effect was detected.

The background, Lorentz, and polarization corrections were introduced into the intensities, as described earlier [44]. We also introduced the Busing and Levy absorption corrections [45] using the linear absorption factors 14.712 mm^{-1} and 14.772 mm^{-1} for MnO at 298 and 85 K, respectively.

The TDS contamination was evaluated by the Merisalo and Kurittu program [46] using the elastic constants from [47]. The effects were small (less than 3% in intensity) because of the high hardness of these compounds.

The observed intensity of a reflection was averaged over the intensities of all the equivalent reflections measured in three experiments.

THE REFERENCE MODEL

Our "direct multipole analysis" is based on the use of a reference model "asymptotically reliable" in the reciprocal space. As far as the condition of asymptotical reliability is fulfilled, the model itself does not affect the interpretation of the results, which can be expressed in terms of the deviations of the experimental charge-density characteristics from those of the model or, when added to the model values, in terms of purely experimental values of these characteristics [41]. In calculations of the model values, an asymptotically fitted Gaussian representation of the theoretical atomic factors can be used to account for the residual terms [48].

According to the conventional rigid-core assumption, the asymptotical reliability can be achieved within sufficient accuracy by using the current theoretical free-atom scattering factors with the appropriate atomic positions and motion parameters. For this purpose, the model should be refined to find the values of these parameters and, at the same time, to bring the observed structure factors to the absolute scale and correct them for extinction and anomalous scattering.

For Mn^{2+}, the relativistic Hartree–Fock values from the International Tables for Crystallography [49] were used and for O^{2-}, the atomic scattering factors suggested by Sanger [50] and the anomalous scattering factors $f' = 0.295$ and $f'' = 0.729$ for Mn^{2+} and $f' = 0.008$ and $f'' = 0.006$ for O^{2-} suggested by Cromer and Liberman [51] (MoK_α).

The structure factors were scaled to the fcc unit cell with four molecules with the origin of the representation being taken at the cation position. The atomic positions (0, 0, 0) and (1/2, 0, 0) for Mn^{2+} and O^{2-} are fixed by the crystal symmetry and have the cubic site symmetry $m3m$. Thus, we have to refine the isotropic Debye–Waller factors of the two ions.

In principle, the refinement can be performed either as a local Fourier-refinement of the difference densities at the atomic positions or as an "asymptotic" least-squares refinement of the structure factors at high $\sin\theta/\lambda$ values.

Since no procedure has been developed to include the extinction parameters in our iterative local Fourier refinement, at the first stage, we used the Linex program written by Becker and Coppens [52] to refine the extinction model together with the scale and the Debye–Waller factors.

All the possible combinations of the extinction models were tried—isotropic and anisotropic, mosaic-spread and particle-size type, with and without primary extinction. Isotropic mosaic-spread extinction gave a lower R factor, 0.005 and 0.004, than the particle-size extinction, 0.006 and 0.005 for MnO at 298 K and 85 K, respectively, and yielded the values $0.032(2) \times 10^4$ rad^{-1} and $0.039(2) \times 10^4$ rad^{-1} for the mosaic spread parameter g and $B(Mn) = 0.300(16)$ $Å^2$, $B(O) = 0.395(47)$ $Å^2$ and $B(Mn) = 0.260(16)$ $Å^2$, $B(O) = 0.379(47)$ $Å^2$, for the iso-

Table 1a. Structure factors for MnO at 298 K

h k l	2sinθ/λ, Å^{-1}	F_0	F_c	δF_0	*y*
0 0 0	0.0000		132		
1 1 1	0.3909	51.83	52.51	0.27	0.894
2 0 0	0.4514	93.21	92.99	0.41	0.704
2 2 0	0.6383	73.48	73.86	0.34	0.869
3 1 1	0.7485	39.88	40.79	0.18	0.959
2 2 2	0.7818	62.69	61.96	0.28	0.929
4 0 0	0.9027	54.41	53.80	0.22	0.953
3 3 1	0.9837	33.33	32.41	0.15	0.983
4 2 0	1.0093	47.11	47.87	0.19	0.962
4 2 2	1.1056	43.50	43.39	0.17	0.974
3 3 3	1.1727	27.71	27.11	0.14	0.991
5 1 1	1.1727	27.10	27.11	0.12	0.990
4 4 0	1.2766	37.35	37.09	0.13	0.985
5 3 1	1.3352	23.48	23.59	0.07	0.992
4 4 2	1.3541	35.45	34.79	0.18	0.987
6 0 0	1.3541	34.98	34.79	0.16	0.985
6 2 0	1.4273	32.93	32.87	0.13	0.988
5 3 3	1.4799	21.40	21.13	0.07	0.994
6 2 2	1.4970	30.69	31.22	0.12	0.990
4 4 4	1.5636	30.72	29.78	0.14	0.991
5 5 1	1.6117	19.10	19.30	0.10	0.996
7 1 1	1.6117	18.90	19.30	0.09	0.995
6 4 0	1.6274	28.37	28.51	0.09	0.990
6 4 2	1.6888	27.31	27.36	0.01	0.991
5 5 3	1.7335	17.81	17.84	0.08	0.996
7 3 1	1.7335	17.99	17.84	0.07	0.996
8 0 0	1.8055	25.22	25.36	0.10	0.993

Table 1b. Structure factors for MnO at 85 K

h k l	2sinθ/λ, Å^{-1}	F_0	F_c	δF_0	*y*
0 0 0	0.0000		132		
1 1 1	0.3914	51.97	52.59	0.30	0.874
2 0 0	0.4520	93.47	93.16	0.40	0.661
2 2 0	0.6392	74.14	74.15	0.15	0.858
3 1 1	0.7495	40.93	41.01	0.18	0.954
2 2 2	0.7828	62.89	62.36	0.30	0.914
4 0 0	0.9039	54.50	54.28	0.19	0.943
3 3 1	0.9851	33.45	32.73	0.14	0.980
4 2 0	1.0106	48.40	48.41	0.19	0.959
4 2 2	1.1071	43.69	43.99	0.18	0.968
3 3 3	1.1743	27.98	27.49	0.12	0.989
5 1 1	1.1743	27.56	27.49	0.12	0.988
4 4 0	1.2784	37.99	37.79	0.18	0.981
5 3 1	1.3370	23.54	24.04	0.10	0.992
4 4 2	1.3559	35.61	35.54	0.16	0.984
6 0 0	1.3559	35.31	35.54	0.19	0.982
6 2 0	1.4293	33.44	33.66	0.12	0.985
5 3 3	1.4819	22.38	21.63	0.11	0.994
6 2 2	1.4990	31.73	32.05	0.10	0.987
4 4 4	1.5657	30.89	30.65	0.15	0.988
5 5 1	1.6139	20.40	19.85	0.10	0.995
7 1 1	1.6139	19.33	19.85	0.10	0.995
6 4 0	1.6296	29.29	29.42	0.15	0.990
6 4 2	1.6911	28.59	28.31	0.14	0.988
5 5 3	1.7359	17.98	18.44	0.10	0.995
7 3 1	1.7359	18.52	18.44	0.09	0.996
8 0 0	1.8079	26.01	26.36	0.10	0.991

tropic Debye–Waller factors at 298 and 85 K, respectively. No more significant improvement was achieved when using any of the more sophisticated models.

The "experimental" structure factors thus obtained were then used as the initial values for a further iterative local Fourier-refinement of the scale and the Debye–Waller factors (cf. [53]). The data obtained at 298 K lead to a further change in the scale by 0.2%, while the scale factor for the data obtained at 85 K remained unchanged. The final refined values, B(Mn) = 0.305 Å^2, B(O) = 0.426 Å^2 and B(Mn) = 0.257 Å^2, B(O) = 0.368 Å^2, were adopted as the Debye–Waller factors of the reference model at 298 and 85 K, respectively.

The refinement also yields experimental structure factors F_0 on an absolute scale corrected for isotropic mosaic-spread extinction and anomalous dispersion. In what follows, these values, listed in Table 1 together with the extinction factors δF_0^2, are subjected to the multipole analysis. The uncertainties F_0 in the table are the standard errors of the mean.

To verify the nature of the residual experimental information, a number of refinement cycles of the Debye–Waller factors were performed for partial data, where the higher order reflections above different cut-off values of sinθ/λ were omitted, with the scale factor fixed at the value found with the total set of the data. It was found that, with increasing cut-off value, the thermal parameters smoothly approach their final values and remain stable beyond 0.8 Å^{-1}. This suggests that, beyond that limit, the X-ray data cannot give the deviations of the ionic formfactors from their theoretical values. Thus, the higher order reflections do not contain any further information on the electronic deformations and are not used in the subsequent multipole analysis.

RESULTS

Once the reference model has been fixed, the calculations required for the multipole analysis of atomic-charge densities can be straightforwardly performed. The principles of the analysis were considered earlier in different contexts [5, 44, 54–56]. Each i atom is discussed separately on the basis of the site-symmetric multipole expansion of the crystal charge-density centered at the atom site

$$\rho_i(\mathbf{r}) = \sum_n \rho_{in}(r_i)K_n(\theta, \varphi),$$

where r_i denotes the radial distance from the atomic site, and on the basis of the corresponding form factor expansion

$$f_i(\mathbf{b}; R_i) = \sum_n f_{in}(b; R_i)K_n(\theta, \varphi),$$

which is the Fourier transform of the charge-density expansion cut at a computational spherical-partitioning radius R_i of the ion. K_n are the cubic harmonics O_e corresponding to the point symmetry $m3m$ [58], and the angular variables θ and φ refer to the local axes, which, in this case, are parallel to the axes of the cubic crystal.

Figure 1 shows the radial accumulation-of-charge densities

$$s_{i0}(r_i) = 4\pi\rho_{i0}(r_i)r_i^2$$

and the radial electron counts

$$Z_{i0}(R_i) = \int_0^{R_i} s_{i0}(r)dr$$

around the ionic sites.

Table 2 is related to Fig. 1 and gives the following spherical characteristics of the ionic charge distributions:

(1) The radii r_0 of best separation at which the radial accumulation-of-charge densities r_0 reach their minima as a measure of the size or the effective "range" of the ionic charge distribution;

(2) the corresponding minimum radial density $s_{0\min} = s_0(r_0)$ as a measure of the nonseparability of the ion from its surroundings;

(3) the electron count $Z_0 = Z_0(r_0)$ within the radius of best separation, as a measure of the charge concentrated in the main bulk of the ionic charge density peak; and

(4) the radii r_{2+} and r_{2-}, where the electron counts reach the values $23e$ and $10e$ corresponding to the doubly ionized states.

Figure 2 presents the radial multipolar scattering factors $f_{in}(b; R_i)$ as deviations from the reference model. The partitioning radii $R_{Mn} = 1.25$ Å and $R_O = 1.30$ Å were deduced on the basis of Fig. 1 and were assumed to be slightly larger than the radii r_0 of best separation [59].

Because of the normalization of the cubic harmonics to the maximum value, 1, the curves directly show the maximum contribution (to be multiplied by 4 for an fcc unit cell) of the component to the structure factors of the crystal as a function of the reciprocal-vector magnitude $b = 2\sin\theta/\lambda$. Their error bars indicate also the significance of the components with respect to the errors of the mean of the structure factors. All the components up to the 10th order were calculated. The first three nonspherical components of orders 4, 6, and 8 are of about the same significance, while the 10th-order component is insignificant and, therefore, is not shown.

For visualization and easier interpretation, the same components are also represented in real space in terms of the multipolar accumulation-of-charge densities $s_{in}(r_i) = B_n\rho_{in}(r_i)r_i^2$ around the ionic sites shown in Fig. 3. Again, the curves represent the deviations from the reference model. The normalization constants $B_n = \int_{K_n>0} K_n(\theta, \varphi)d\Omega$ [53] ensure that the areas under the curves give the electron counts under the positive lobes of $K_n(\theta\varphi)$ within the radii R_i. These multipolar electron counts serve as nonspherical integral characteristics of the ionic charge distributions, as is indicated by the numbers in the figures.

The results are visualized in Fig. 4 in terms of difference-density maps representing the multipole expansions at the ionic sites, as composed by the components shown in Figs. 2 and 3. For each ion map, the three main lattice planes (100), (110) and (111) passing through the ionic site are shown.

For comparison, the conventional Fourier difference-density maps in the same planes are shown. Finally, views on the 3-dimensional nature of the ionic multipole expansions are shown in Fig. 5 to support the discussion of results.

DISCUSSION

The comparison of the radial densities s_0 of the reference model at two different temperatures presented by the dotted lines in Fig. 1 and by the corresponding parameters in Table 2 shows that the effect of the temperature factors on the nature of the ionic-charge distributions is negligible. Thus, the differences in the character of the experimental curves and the parameters at the two temperatures are of electronic origin and can be attributed to the differences in the magnetic states. They are evident from the deviations of the experimental curves from the reference curves in Fig. 1 and in the numerical values listed in Table 2. On a larger scale, they are shown by the Δs_0 curves in Fig. 3.

The radial density $s_0(r)$ in the region of overlap around the oxygen atom is obviously reduced in comparison with that for the reference model. The peaks are compressed and the minima are sharpened, thus improving the separation of the atoms from their sur-

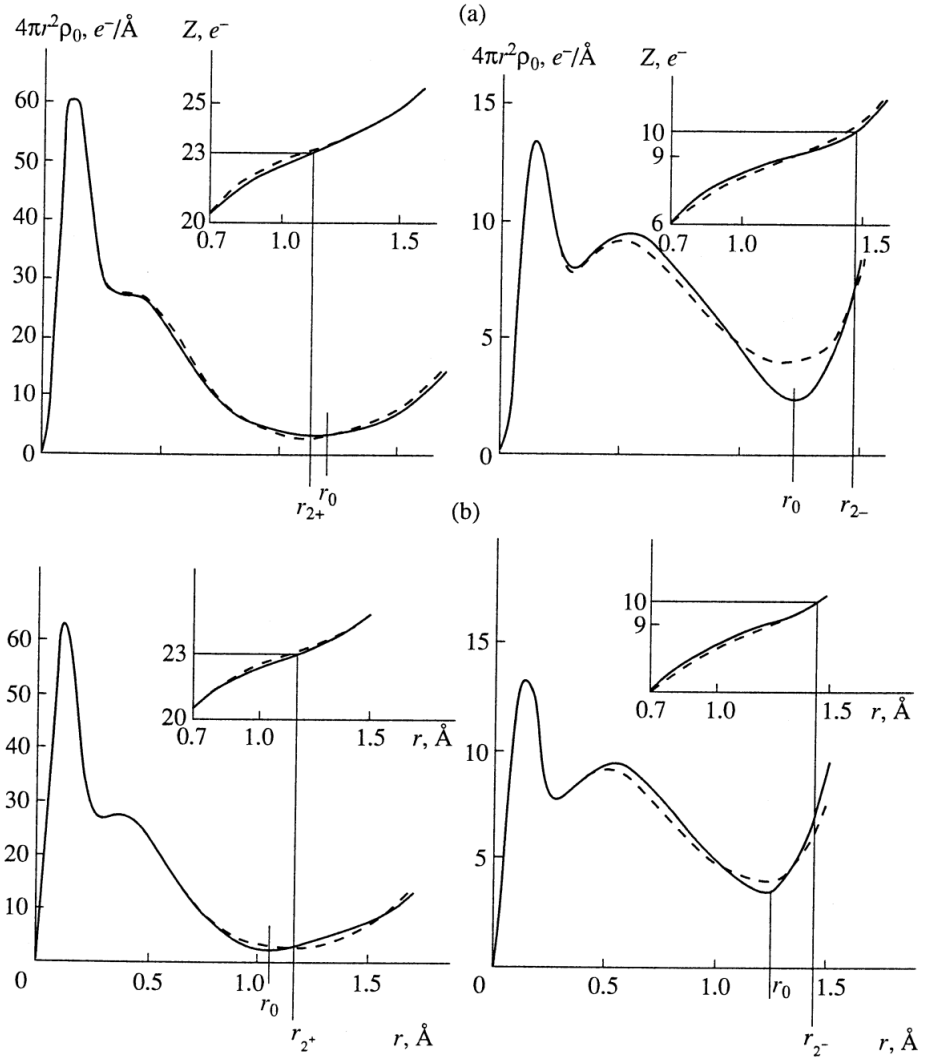

Fig. 1. Radial accumulation-of-charge densities $s_0(r)$ and electron counts $Z_0(r) = s_0(r)dr$ around the ionic sites of Mn^{2+} and O^{2-}, solid lines—experiment, dashed lines—reference model. (a) The paramagnetic state (298 K), (b) the antiferromagnetic state (85 K). The radii r_0 of the "best separation" or minimum s_0 and the radii r_{2^+} and r_{2^-}, where the electron counts corresponding to the double ionization of the ions are indicated for the experimental curves.

roundings and yielding well-defined radii of best separation of the ions from their surroundings. These features typical of ionic crystals [44, 53] are exceptionally strong in the paramagnetic state. In both states, the oxygen peak is about $9e$, a value known for several other oxides [54, 57]. The radius r_{2^-} corresponding to the double ionization of oxygen or $10e$ is obviously larger, thus indicating that the tenth electron is distributed in a wider region between the main density peaks.

In manganese, the deviations from the reference model are of a different nature. In the antiferromagnetic state, the "ionic" sharpening of the separating minima is seen. However, it is caused by a slight expansion of the outer part of the ion. In the paramagnetic state, the minimum is flattened because of a somewhat inner expansion leading to a rather undetermined separation radius and to a higher value of the minimum density, which is more typical of covalent bonding. The electron counts indicated in Table 2 differ only because of the different radii used. In both states, the electron count of the manganese peak is very close to $23e$ corresponding to double ionization.

It should also be noted that the radial accumulation-of-charge densities at the minima are essentially higher than could be expected for an ionic crystal (cf. [54] and [44]). Manganese and oxygen in paramagnetic MnO have the highest and the least values, respectively. Both

Table 2. Spherical characteristics of the ionic electron distributions: radius r_0 of the best separation at which the radial accumulation-of-charge density $s_0(r)$ reaches its minimum; the minimum radial density $s_{0\min} = s_0(r_0)$; the electron count $Z_0 = Z_0(r_0)$ within the radius of the best separation, and the radii r_{2+} and r_{2-}, where the electron counts reach the values $23e$ and $10e$ corresponding to the doubly ionized states

Mn^{2+}	r_0	$s_{0\min}$	Z_0	r_{2+}
experiment				
298 K	1.20 Å	4.42 *e*/Å	23.34 *e*	1.12 Å
85 K	1.05 Å	3.23 *e*/Å	22.59 *e*	1.16 Å
reference model				
298 K	1.15 Å	3.57 *e*/Å	23.15 *e*	1.11 Å
85 K	1.10 Å	3.57 *e*/Å	22.97 *e*	1.10 Å
O^{2-}	r_0	$s_{0\min}$	Z_0	r_{2-}
experiment				
298 K	1.22 Å	2.61 *e*/Å	9.00 *e*	1.47 Å
85 K	1.25 Å	3.75 *e*/Å	9.21 *e*	1.45 Å
reference model				
298 K	1.20 Å	4.13 *e*/Å	8.80 *e*	1.44 Å
85 K	1.20 Å	4.20 *e*/Å	8.80 *e*	1.44 Å

these values pronouncedly change in the transition to the antiferromagnetic state, but along different directions.

The above differences indicate the exchange of the roles of the two ions as a result of the magnetic phase transition. The nonspherical radial accumulation-of-charge densities $\Delta s_n = 4.6$ and 8 in Fig. 3 throw some further light on their 3-dimensional nature.

Considering the angular behavior of the cubic harmonics schematically presented in Figs. 2 and 3 (cf. [60]), it is possible to note that at distances with positive values of $\Delta(r)$, the 4th-order component transfers electrons from the ⟨111⟩ to the ⟨100⟩ directions, the 6th-order component from the ⟨110⟩ mainly to the ⟨111⟩ and, to a somewhat lesser extent, to the ⟨100⟩ directions, while the 8th-order component collects electrons rather sharply to the ⟨100⟩ and, to some extent, also to the ⟨110⟩ directions from the intermediate directions. For negative values of $\Delta(r)$, the transfer has the opposite sense. Thus, considering the sign combinations in the inner and outer regions and comparing them, one can roughly deduce the 3-dimensional nature of the combined components to be related to the nature of the different electronic effects in two atoms in two magnetic states.

Here, the map representations in Fig. 4 give important support. However, it should be noted that, in the local map representations, only those features are significant which are significant in the angular-integral representation in Fig. 3. Thus, the difference densities at the ionic centra in any of the maps can be ignored. Similarly, no local features of the Fourier maps that are not seen in the multipolar maps in Fig. 4 can arise from the integral systematics of the low-order multipoles and, thus, can be regarded insignificant. The comparison with the multipolar maps allows us to follow how features seen in the Fourier maps originate from the electronic behavior of different atoms [41].

In paramagnetic MnO, the most striking feature is the concentration of electrons in the Mn^{2+} ion in the twelve equivalent ⟨110⟩ directions. This is clearly seen from all the maps constructed through the Mn site, because they have a common ⟨110⟩ line. In the Fourier maps, this can give rise to bondlike concentrations of electrons indicating the electronic Mn–Mn interactions between each Mn ion with its twelve Mn neighbors. This explains the flattening of the separating minimum of the radial density in Fig. 1.

The origin and nature of this formation is somewhat unclear. In the Mn multipole maps, the formation seems to be caused mainly by the electrons of the Mn ions participating in both internal and external coupling. However, it extends beyond the radius r_{2+} of double ionization. Nevertheless, the formation is also visible in the oxygen multipole maps, which is obvious from the comparison of the multipole and the Fourier maps in the (100) and (110) planes, where it is seen to bridge the neighboring oxygen atoms. In the 3-dimensional view in Fig. 5, it appears as a cage surrounding an oxygen ion. In the periodic crystal structure, these cages build up a 3-dimensional net with a pocket for each oxygen atom. Therefore, although this formation lies beyond any reasonable separating radius, the oxygen ion probably plays a certain role in its formation. Then, some electronic Mn–O interactions should be involved. There should also be the space to hide the "lacking tenth electron" of O^{2-}.

The formation of a net structure is a parallel phenomenon to the formation of an oxygen net structure observed in beryllium oxide [5]. A closer look at the results of the multipole analysis of some other oxides [54] shows that the formation of such interatomic nets might be a more general phenomenon in oxides.

In addition, the multipole maps show the significant deformation of both ions. In oxygen, this appears as an additional concentration of electrons in the ⟨100⟩ directions. In manganese ions, the charge density is significantly reduced in these directions. These features are similar in nature to the ionic deformations observed in ionic crystals [44, 54]. While they are caused by electrostatic cation–anion interactions, they are electronically internal features of each ion.

The peak that appears on the (110) Fourier map at the empty 1/4, 1/4, 1/4 position is a local feature that cannot be attributed to any systematic integral behavior of the charge density. In integration, it is found to be an accumulation of 0.016 electrons only, i.e., is negligible. Thus, it is a typical artefact of the local Fourier representation.

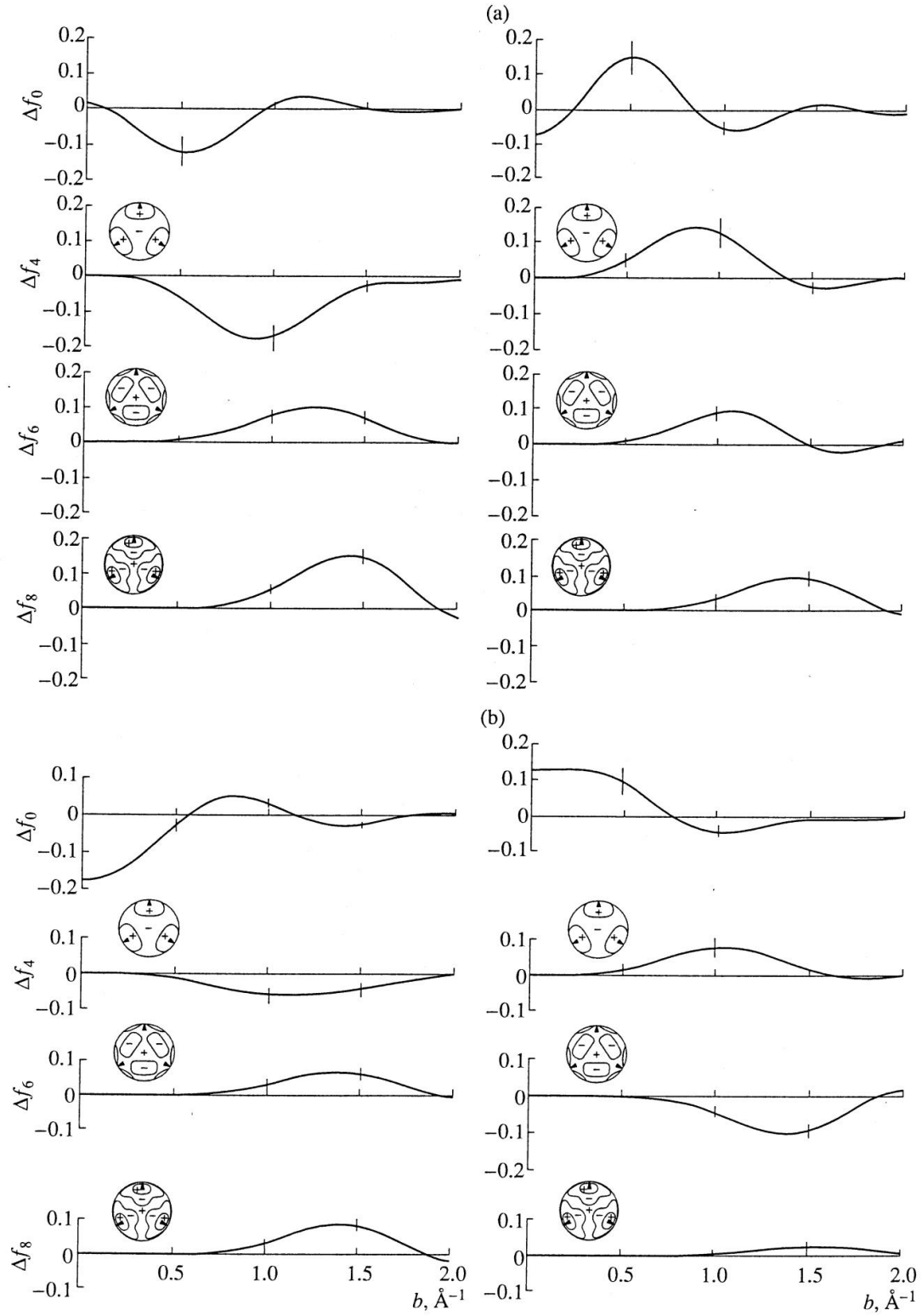

Fig. 2. Radial multipolar scattering factors of the Mn^{2+} and O^{2-} ions within the partitioning radii R_{Mn} = 1.25 Å, R_O = 1.30 Å. The results are related to cubic harmonics normalized to the maximum value $K_n(\theta\varphi) = 1$, and the curves represent the deviations Δf_n from the reference model. (a) The paramagnetic state (298 K), (b) the antiferromagnetic state (85 K).

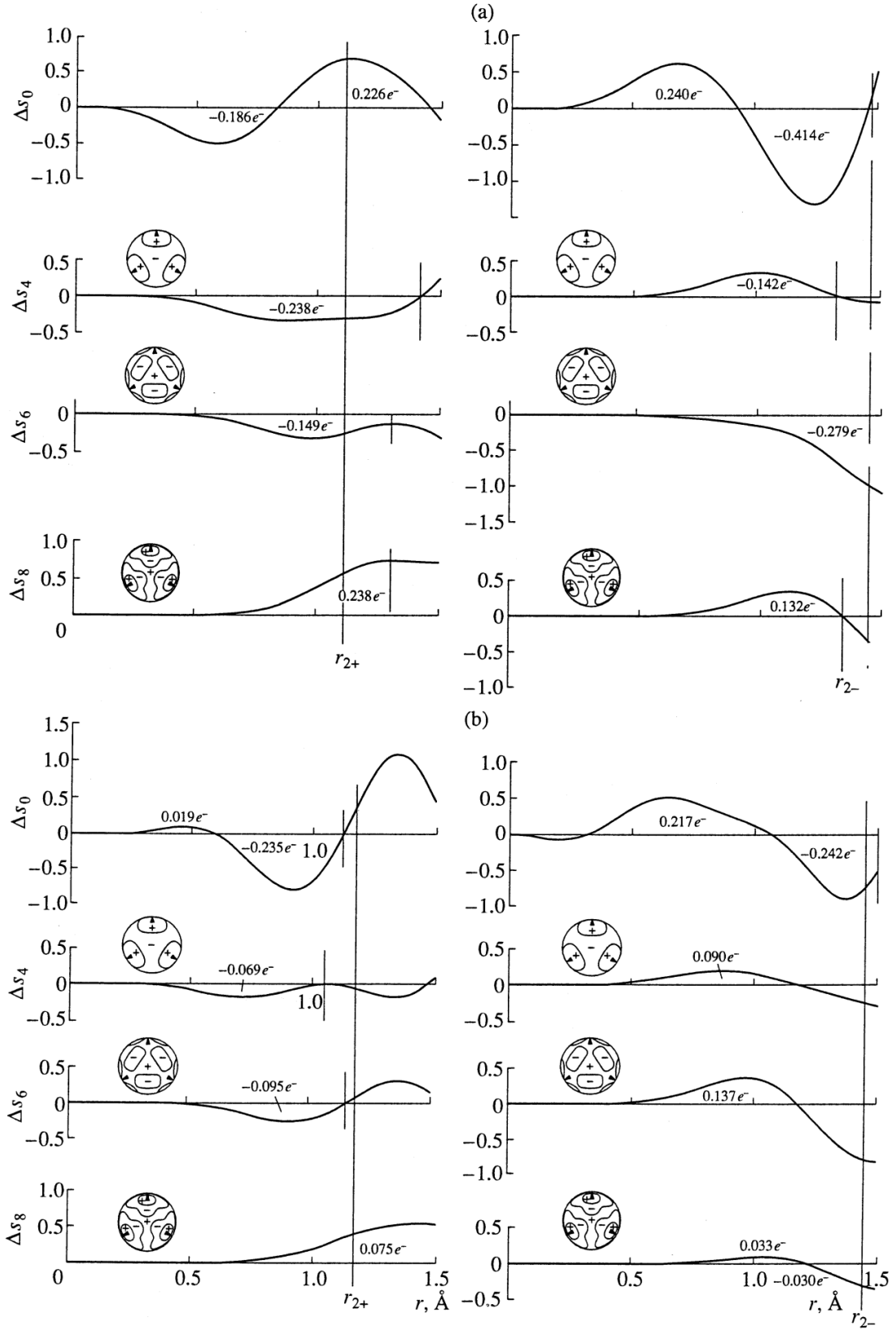

Fig. 3. Multipolar accumulation-of-charge densities $s_n(r)$ around the ionic sites of Mn^{2+} and O^{2-}. The curves represent deviations Δs_n from the reference model. (a) The paramagnetic state (298 K), (b) the antiferromagnetic state (85 K).

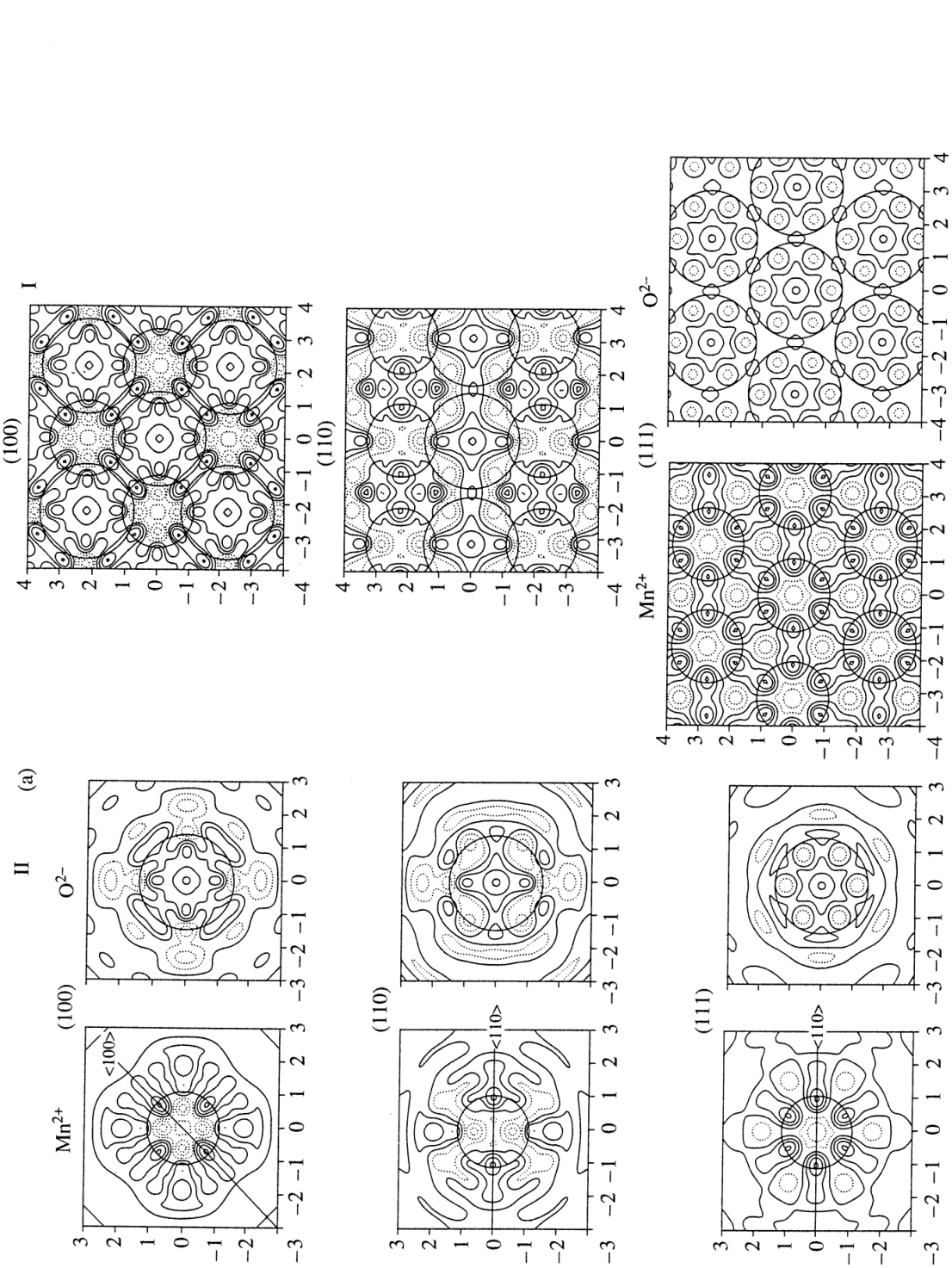

Fig. 4. Difference density maps of the multipole expansions up to $n = 8$ together with the corresponding Fourier difference-density maps on the (100), (110), and (111) planes passing through the ionic sites. Circles indicate the radii of doubly ionized ions. (a) The paramagnetic state (298 K), (b) the antiferromagnetic state (85 K). Solid lines indicate positive, dashed lines indicate negative, and dotted lines indicate zero values; the contours are spaced by 0.1 eÅ^{-3}.

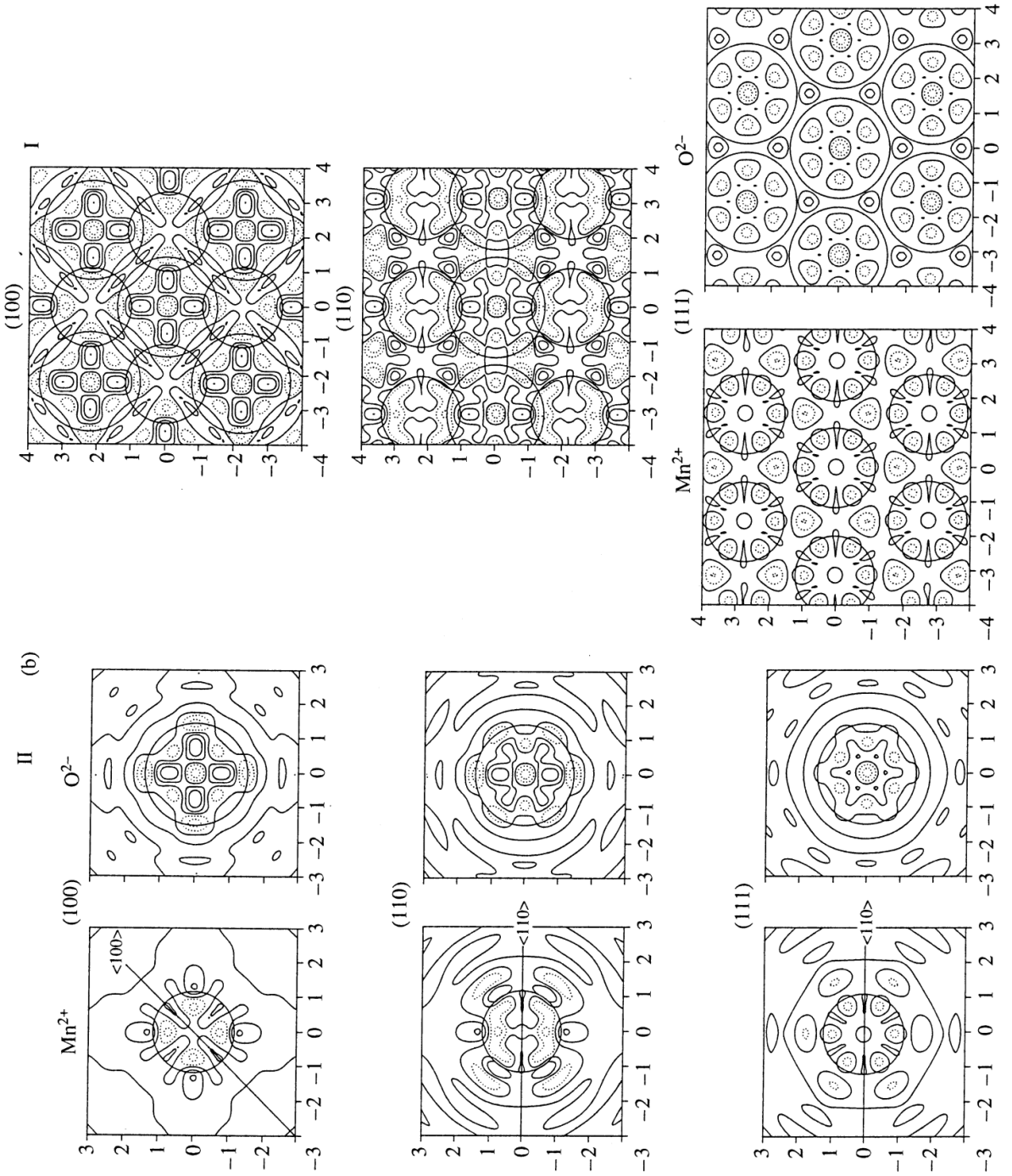

Fig. 4. (Contd.)

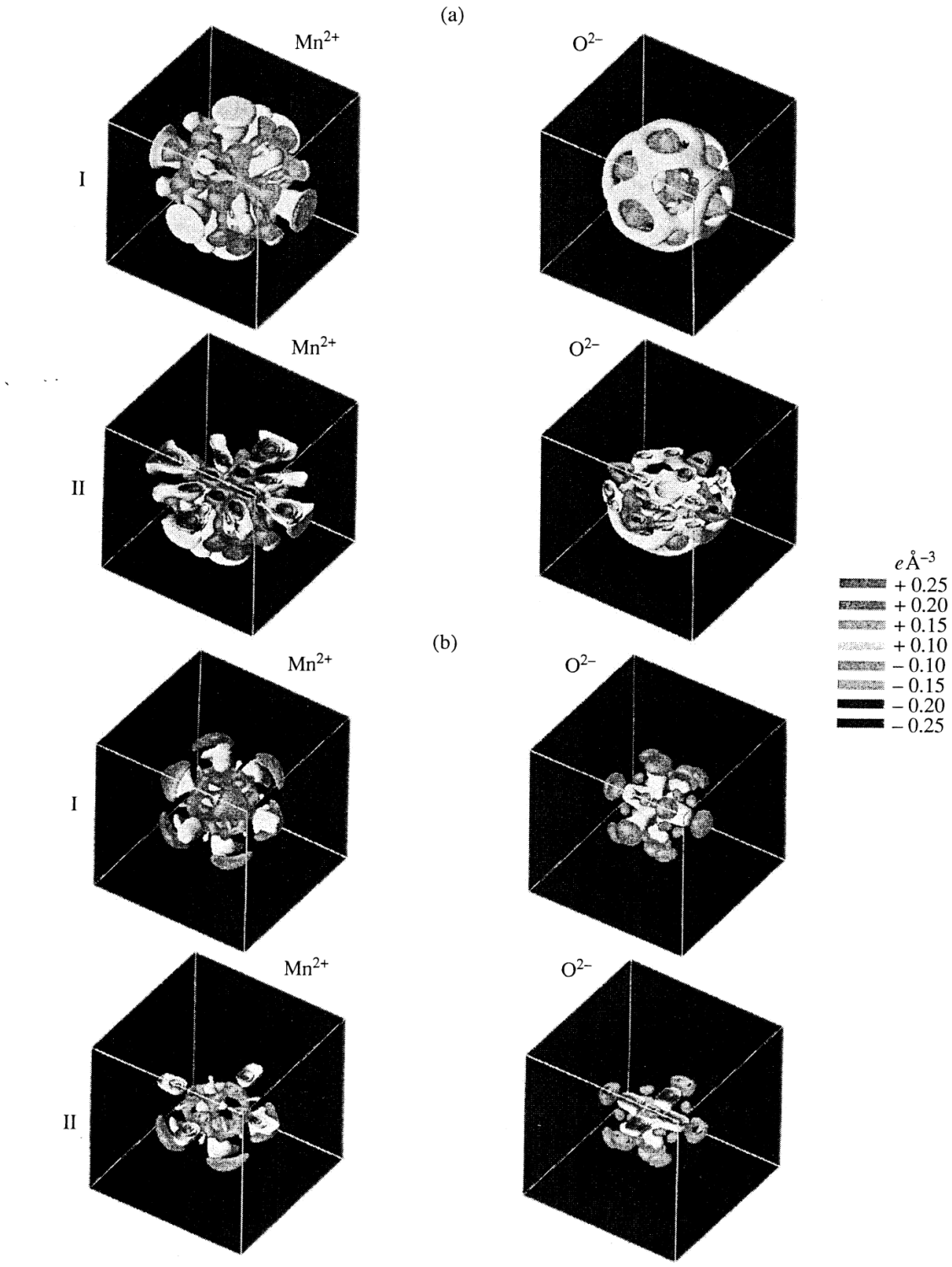

Fig. 5. Three-dimensional view on the ionic multipole expansions, extracts from a video presentation of the 3-dimensional distributions of MnO [61]. Surface-representations +0.1 and –0.1 eÅ^{-3} and section-representations +0.25 to –0.25 eÅ^{-3}; the zero value is omitted. Contours are spaced by 0.05 eÅ^{-3}. (a) The paramagnetic state (298 K), (b) the antiferromagnetic state (85 K).

The most obvious changes caused by the transition to the antiferromagnetic state is the disappearance of strong Mn–Mn bonding. There are some traces of such bonding, but the effect is much weaker than in the paramagnetic state. Now, there is no bridging between oxygen atoms, and it is unclear whether the net formation is still continued, although the areas of low but continuous additional charge density surrounding the oxygen in the multipolar maps and on the (111) Fourier map give a slight indication that the net formation still proceeds.

The general appearance of the deformations attributed to the electrostatic cation–anion interaction have not changed essentially. In manganese, they are weaker, as can be seen from the reduction of the 4th- and 6th-order radial densities (Fig. 3). In oxygen, these components interchanged their roles, which leads to the general impression that the effect has become somewhat stronger. This and the obviously higher minimum value of the spherical density in Fig. 1 indicate the presence of some electronic O–Mn coupling.

The combination of two positive and two negative peaks around the empty 1/4, 1/4, 1/4 position on the (110) Fourier map is a local feature and an obvious artefact.

REFERENCES

1. J. Kübler and A. R. Williams, J. Magn. Magn. Mater. **54–57**, 603 (1986).
2. S. Hüufner, Adv. Phys. **43** (2), 183 (1994).
3. M. S. Jagadeesh and M. S. Seehra, Phys. Rev. B **23** (3), 1185 (1981).
4. G. Srinivasan and M. S. Seehra, Phys. Rev. B **28** (11), 6542 (1983).
5. D. Seino, J. Magn. Magn. Mater. **28**, 55 (1982).
6. M. S. Seehra and R. E. Helmick, Phys. Rev. B **24** (9), 5098 (1981).
7. M. S. Seehra, R. E. Helmick, and G. Srinivasan, J. Phys. C **19**, 1627 (1986).
8. Ya. M. Ksendzov, I. L. Korobova, K. K. Sidorin, and G. P. Startsev, Fiz. Tverd. Tela (Leningrad) **18** (1), 173 (1976) [Sov. Phys. Solid State **18**, 99 (1976)].
9. N. A. Drokin, S. G. Ovchinnikov, and L. I. Ryabinkina, Fiz. Tverd. Tela (Leningrad) **29** (6), 1625 (1987) [Sov. Phys. Solid State **29**, 935 (1987)].
10. R. J. Lad and V. E. Henrich, Phys. Rev. B **38** (15), 10860 (1988).
11. S. Mochizuki, B. Piriou, and J. Dexpert-Ghys, J. Phys.: Condens. Matter **2**, 5225 (1990).
12. A. Fujimori, N. Kimizuka, T. Akahane, *et al.*, Phys. Rev. B **42** (12), 7580 (1990).
13. J. M. McKay and V. E. Henrich, Phys. Rev. Lett. **53** (24), 2343 (1984).
14. G. A. Sawatzky and J. W. Allen, Phys. Rev. Lett. **53** (24), 2339 (1984).
15. S. Hüfner, J. Osterwalder, T. Riesterer, and F. Hulliger, Solid State Commun. **52** (9), 793 (1984).
16. E. Zschech, L. Troger, D. Arvanitis, *et al.*, Solid State Commun. **82** (1), 1 (1992).
17. K. S. Kim, Phys. Rev. B **11** (6), 2177 (1975).
18. T. Van Elp, J. L. Wieland, H. Eskes, *et al.*, Phys. Rev. B **44** (12), 6090 (1991).
19. K. Okada and A. Kotani, J. Phys. Soc. Jpn. **61** (2), 449 (1992).
20. J. Kanamori, J. Phys. Chem. Solids **10**, 187 (1959).
21. L. F. Mattheiss, Phys. Rev. B **5** (2), 306 (1972).
22. K. Terakura, T. Oguchi, A. R. Williams, and J. Kübler, Phys. Rev. B **30** (8), 4734 (1984).
23. K. Terakura, A. R. Williams, T. Oguchi, and J. Kübler, Phys. Rev. Lett. **52** (20), 1830 (1984).
24. J. Hugel and C. Carabatos, Solid State Commun. **60** (4), 369 (1986).
25. V. J. Anisimov, M. A. Korotin, and E. Z. Kurmaev, J. Phys.: Condens. Matter **2**, 3973 (1990).
26. A. E. Bocquet, T. Mizokawa, T. Saitoh, *et al.*, Phys. Rev. B **46** (7), 3771 (1992).
27. W. Nolting, L. Haunert, and G. Borstel, Phys. Rev. B **46** (8), 4426 (1992).
28. V. J. Anisimov, P. Kuiper, and J. Nordgren, Phys. Rev. B **50** (12), 8257 (1994).
29. W. L. Roth, Phys. Rev. **110** (6A), 1333 (1958).
30. W. L. Roth, Phys. Rev. **111** (3B), 772 (1958).
31. D. Bloch, R. Maury, C. Vetter, and W. B. Yelon, Phys. Lett. A **49 A** (5), 354 (1974).
32. H. Shaked, J. Faber, and R. L. Hittrman, Phys. Rev. B **38** (16), 11901 (1988).
33. D. Hermann-Ronzaud, P. Burlet, and J. Rossat-Mignot, J. Phys. C **11**, 2123 (1978).
34. H. Chang, J. F. Harrison, T. A. Kaplan, and S. D. Mahanti, Phys. Rev. B **49** (22), 15753 (1994).
35. M. Kuriyama and S. Hosoya, J. Phys. Soc. Jpn. **17** (6), 1022 (1962).
36. R. Uno, J. Phys. Soc. Jpn. **20** (3), 308 (1965).
37. V. Meisalo and O. Inkinen, Ann. Acad. Sci. Fenn., Ser. A6 **240**, 4 (1967).
38. S. Sasaki, K. Fujino, Y. Takeuchi, and R. Sadanaga, Acta Crystallogr., Sect. A: Cryst. Phys., Diffr., Theor. Gen. Crystallogr. **36**, 904 (1980).
39. J.-P. Vidal, in *Symposium Franco–Finlandais. Structure de la Matiere. Reparitions Electroniques dans les Cristaux, Paris, 1993*, Ed. by J.-P. Vidal (Montpellier, 1994), p. J1.
40. G. Vidal, in *Symposium Franco–Finlandais. Structure de la Matiere. Reparitions Electroniques dans les Cristaux, Paris, 1993*, Ed. by J.-P. Vidal (Montpellier, 1994), p. I1.
41. K. Kurki-Suonio, in *Symposium Franco–Finlandais. Structure de la Matiere. Reparitions Electroniques dans les Cristaux, Paris, 1993*, Ed. by J.-P. Vidal (Montpellier, 1994), p. F1.
42. J.-P. Vidal, G. Vidal-Valat, and C. M. E. Zeyen, Nucl. Instrum. Methods **228**, 569 (1985).
43. A. Revcolevschi, Rev. Int. Hautes Temp. Refract. **7**, 73 (1970).

44. J.-P. Vidal, G. Vidal-Valat, M. Galtier, and K. Kurki-Suonio, Acta Crystallogr., Sect. A: Cryst. Phys., Diffr., Theor. Gen. Crystallogr. **37**, 826 (1981).
45. W. R. Busing and H. A. Levy, Acta Crystallogr. **10**, 180 (1957).
46. M. Merisalo and J. Kurittu, J. Appl. Crystallogr. **11**, 179 (1978).
47. K. G. Subhadra and D. B. Sirdeshmukh, Indian J. Pure Appl. Phys. **16**, 693 (1978).
48. R. Sälke and K. Kurki-Suonio, *Report Series in Physics* (Univ. of Helsinki, 1984), HU-P-233.
49. *International Tables for X-ray Crystallography* (Kluwer, Dordrecht, 1999), Vol. C.
50. P. L. Sanger, Acta Crystallogr., Sect. A: Cryst. Phys., Diffr., Theor. Gen. Crystallogr. **25**, 694 (1969).
51. D. T. Cromer and D. Liberman, J. Chem. Phys. **53**, 1891 (1970).
52. P. J. Becker and P. Coppens, Acta Crystallogr., Sect. A: Cryst. Phys., Diffr., Theor. Gen. Crystallogr. **31**, 417 (1975).
53. G. Vidal-Valat, J.-P. Vidal, K. Kurki-Suonio, and R. Kurki-Suonio, Acta Crystallogr., Sect. A: Found. Crystallogr. **48**, 46 (1992).
54. G. Vidal-Valat, J.-P. Vidal, and K. Kurki-Suonio, Acta Crystallogr., Sect. A: Cryst. Phys., Diffr., Theor. Gen. Crystallogr. **34**, 594 (1978).
55. K. Kurki-Suonio and R. Sälke, in *Local Density Approximations in Quantum Chemistry and Solid State Physics*, Ed. by J. P. Dahl and J. Avery (Plenum, New York, 1984), p. 713.
56. K. Kurki-Suonio and R. Sälke, Kristallografiya **31**, 776 (1986) [Sov. Phys. Crystallogr. **31**, 458 (1986)].
57. G. Vidal-Valat, J.-P. Vidal, K. Kurki-Suonio, and R. Kurki-Suonio, Acta Crystallogr., Sect. A: Found. Crystallogr. **43**, 540 (1987).
58. M. Kara and K. Kurki-Suonio, Acta Crystallogr., Sect. A: Cryst. Phys., Diffr., Theor. Gen. Crystallogr. **37**, 201 (1981).
59. K. Kurki-Suonio, Acta Crystallogr., Sect. A: Cryst. Phys., Diffr., Theor. Gen. Crystallogr. **24**, 379 (1968).
60. J.-P. Vidal, K. Kurki-Suonio, G. Vidal-Valat, and R. Kurki-Suonio, Video-film "Visualization of Spherical, Cubic and Icosahedral Harmonics," Ed. by J.-P. Vidal, Distributed by service du Film de Recherche Scientifique (Vanves, France, 1995).
61. J.-P. Vidal, K. Kurki-Suonio, G. Vidal-Valat, and R. Kurki-Suonio, Video-film "Is It Possible to Visualize the Multipole Expansion in Three Dimensions?," Ed. by J.-P. Vidal, distributed by Service du Film de Recherche Scientifique (Vanves, France, 1993).